# Electrodeposition of tunable Cu-Ag nanostructures in a deep eutectic solvent

Elena Plaza-Mayoral[1*], Kim N. Dalby[2], Hanne Falsig[2], Ib Chorkendorff[3], Paula Sebastián-Pascual[1*], María Escudero-Escribano[*,1,4,5]

(1) Center for High Entropy Alloy Catalysis, Department of Chemistry, University of Copenhagen, Universitetsparken 5, 2100 Copenhagen, Denmark

(2) Topsoe A/S, Haldor Topsøe Allé 1, DK-2800 Kgs. Lyngby, Denmark

(3) Department of Physics, Surface Physics and Catalysis, Technical University of Denmark, Fysikvej, DK-2800 Lyngby, Denmark

(4) Catalan Institute of Nanoscience and Nanotechnology (ICN2), CSIC, Barcelona Institute of Science and Technology, UAB Campus, 08193 Bellaterra, Barcelona, Spain

(5) Catalan Institution for Research and Advanced Studies (ICREA), Pg. Lluís Companys 23, 08010 Barcelona, Spain

*Corresponding authors:

E-mail: maria.escudero@icn2.cat

E-mail: paula.pascual@chem.ku.dk

E-mail: epm@chem.ku.dk

# ABSTRACT

The green transition requires the preparation of clean, inexpensive, and sustainable strategies to prepare controllable bimetallic and multimetallic nanostructures. Cu-Ag nanostructures, for example, are promising bimetallic catalysts for different electrocatalytic reactions such as carbon monoxide and carbon dioxide reduction. In this work, we present the one-step preparation method of electrodeposited Cu-Ag with tunable composition and morphology from choline chloride plus urea deep eutectic solvent (DES), a non-toxic and green DES. We have assessed how different electrodeposition parameters affect the morphology and composition of our nanostructures. We combine electrochemical methods with ex-situ scanning electron microscopy (SEM), energy dispersive X-ray spectroscopy (EDS), and X-ray photoelectron spectroscopy (XPS) to characterize the nanostructures. We have estimated the electrochemically active surface area (ECSA) and roughness factor (R) by lead underpotential deposition (UPD). The copper/silver ratio in the electrodeposited nanostructures is highly sensitive to the applied potential, bath composition, and loading. We observed that silver-rich nanostructures were less adherent whereas the increase in copper content led to more stable and homogenous films with disperse rounded nanostructures with tiny spikes. These spikes were more stable when the deposition rate was fast enough and the molar ratio of Cu and Ag no greater than approximately two to one.

## Keywords

Electrodeposition, deep eutectic solvent, green solvent, copper-silver nanostructures, tunable nanocatalysts.

**Table of contents graphic**
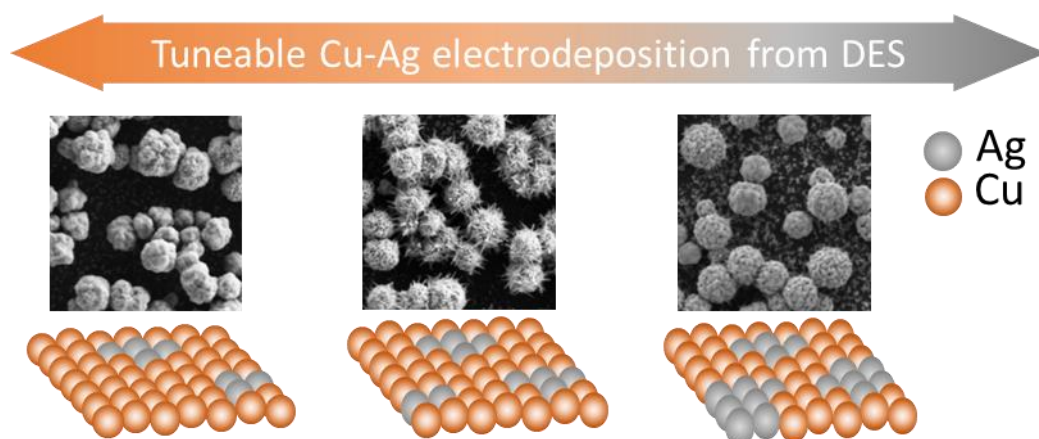


**Introduction**

In our path towards a decarbonized chemical industry, novel electrocatalyst materials for renewable energy conversion have been extensively explored in the last decades.[1–3] There is an increasing demand for affordable and clean strategies to design new sustainable nanomaterials while improving their electrocatalytic properties.[4–7] Nanomaterials account for a high surface-to-area ratio which provides an enhanced number of active sites per unit area for the electrocatalytic reaction to take place actively. The number of active sites per surface area is commonly known as the electrochemically active surface area (ECSA).[8,9] While monometallic nanostructures have been widely investigated, the design of new bimetallic and multimetallic nanostructures is the focus of this study due to the possibility of creating new catalyst with new properties by combining different metals. When combining different metals, we can selectively tune the catalytic properties and binding energies of the key intermediates through the modification of both ligand and strain effects at the catalyst surface.[10–13] Among bimetallic catalysts, Cu-Ag nanocatalysts have shown promising properties towards the oxygen reduction reaction (ORR) in alkaline media and, most commonly, the electrochemical reduction of carbon monoxide and carbon dioxide (CORR and $CO_2RR$).[14–

19] Controlling the size, shape and composition of these NPs is crucial to enhance the activity and tune the selectivity towards the desired product. Multiple physical and chemical synthesis methods have been studied to prepare Cu-Ag catalysts with controlled size, shape and composition.[10,18,20–23] These methods are often time and energy demanding (i.e. sputtering in ultra-high vacuum)[24] or need the addition of surfactants agents to control the growth of the nanoparticles with its subsequent removal step (i.e. colloidal synthesis).[25,26] Therefore, there has been an increase demand for developing new strategies to tailor the properties of these nanostructures in a clean, fast and economically competitive approach. Metal electrodeposition from deep eutectic solvents (DES) has emerged as an inexpensive and green strategy to prepare new bimetallic and multimetallic nanocatalysts in one single step.[27–29]

DES are non-toxic solvents composed by the eutectic mixture of a quaternary ammonium salt and a proton neutral donor molecule. They are soluble in water, have a wide electrochemical window and good conductivity.[30–32] In contrast to metal electrodeposition in aqueous media, this solvent allows us to deposit most of the metals in a controllable way without the addition of any additives and without solvent co-reduction.[28] Metal electrodeposition in aqueous media has been widely explored to prepare multiple alloys and oxides.[33] However, the electrodeposition in aqueous solvents for metals with high negative reduction potentials is often hindered by the hydrogen evolution from the solvent co-reduction, reducing the energy efficiency of the electrodeposition.[34] In addition to that, due to fast deposition kinetics in aqueous solution, undesirable growth mechanisms such as dendritic growth can occur, leading to a non-homogenous deposit with low adherence.[34–36] For the electrodeposition of Cu-Ag in aqueous media, cyanide-based electrolytes or different additives have been commonly used to facilitate the deposition of both metals and to lead the growth of the NPs.[20,21,37] Since cyanide baths are extremely toxic, ammonia-based electrolytes have been proposed as a

cyanide-free alternative for the electrodeposition of Cu-Ag.[38] However, even though ammonia toxicity is lower than cyanide, it is a water contaminant in comparison with the non-toxic DES.[39]. Metal electrodeposition from DES is preferred because we can tailor the size, morphology, and composition of our nanostructures by tuning different parameters and without additional surfactant agents, as DES is both the solvent and the ligand agent. In addition, any traces of DES after the electrodeposition process are easily removed by rinsing with hot water as the DES is soluble in water, is non-toxic and is biodegradable.[30,40–42] These advantages make deep eutectic solvents suitable green solvents for the preparation of new bimetallic nanostructures.

Several studies have proved the use of DES for electrodeposition of bimetallic nanostructures in the last years: CuAu[41], CoPt[43], CuIn[44], CoNi[45], PdAu[42], CuGa[46], CuZn[47] and ZnNi[48]. In one of our previous works, we prepared CuAu nanostructures with tunable morphology and composition by electrodeposition from DES.[41] Malaquias et al. and Steichen et al. investigated the electrodeposition of Cu-In and Cu-Ga alloys, respectively, on a Mo rotating disk electrode using a choline chloride and urea DES solvent.[44,46] Other studies have reported the electrodeposition of CuSn[49], PdAg[50] or AgSn[51] alloys from DES but after incorporating an additive to facilitate the mixture of the metals. These works show that electrodeposition of bimetallic and multimetallic nanostructures from different DES is still emerging, and multiple multimetallic materials with tunable structure could be obtained from DES by changing several parameters such as the proton donor molecule of DES, the temperature, the applied potential, or the bath composition without the need of any additives.

The single Cu and Ag electrodeposition from different DES solvents have also been widely studied. Different groups have shown how single Cu and Ag can be tuned and how they mechanistically behave during electrodeposition from DES as well as on different non-metallic and metallic substrates.[52–60]. Nevertheless, the CuAg electrodeposition from DES has been

5

less explored. Herein, we report the co-electrodeposition of CuAg with tunable composition from a choline chloride plus urea DES on glassy carbon. We have assessed in detail how different parameters affect the morphology and composition of our nanostructures. For that purpose, we have used three different Cu-Ag bath compositions and prepared different loadings at two applied potentials (i.e. two deposition rates). We have used cyclic voltammetry (CV) and chronoamperometry (CA) to electrochemically characterize the electrodeposition process. The morphology and composition were evaluated through ex-situ scanning electron microscopy (SEM), energy dispersive X-ray spectroscopy (EDS) and X-ray photoelectron spectroscopy (XPS). Finally, we have estimated the ECSA and roughness factor (R) of each nanostructure by lead underpotential deposition (UPD) following a similar protocol than in our previous reports.[61] Herein, we present an easy and affordable method to prepare Cu-Ag nanostructures with tunable morphology and composition and in one electrodeposition step.

**Experimental section**

We have analyzed three different Cu-Ag bath solutions. Prior to dissolving the metal salts we prepared the DES from a mixture of choline chloride (ChCl, Across organics, 99%) and urea (Sigma- Aldrich, 99%) with a molar ratio of 1:2. We applied constant manual stirring at 40°C until both salts were totally dissolved and we obtained a colourless deep eutectic solvent. Once the DES was ready, $CuCl_2$ (Sigma-Aldrich, 99%) and AgCl (Sigma-Aldrich, 99 %) salts were dissolved in the DES by magnetic stirring at 60°C overnight. The three bath solutions prepared for the electrodeposition of bimetallic nanostructures were: (a) 0.075 M $CuCl_2$ / 0.025 M AgCl + DES solution, corresponding to 3Cu:1Ag molar ratio solution; (b) 0.086 M $CuCl_2$ / 0.014 AgCl + DES solution, corresponding to 6Cu:1Ag molar ratio solution; (c) 0.05 M $CuCl_2$ / 0.05 M AgCl + DES solution, corresponding to 1Cu:1Ag molar ratio solution.

6

The electrodeposition was performed in a small volume three-electrode cell configuration with a Pt wire as counter electrode, a Ag wire as pseudo reference electrode and a glassy carbon (GC) rod of 5 mm of diameter as the working electrode. The potential values were transformed to the Ag│AgCl reference electrode scale.[52] The counter and reference electrodes were pre-treated by flame-annealed and subsequent rinsing with Milli-Q water (18.2 MΩcm, TOC < 5 ppm). A 30% diluted $HNO_3$ solution was used to remove metallic traces from the counter and reference electrodes followed by rinsing with abundant milli-Q water before the flame-annealing if needed. The GC was pre-treated by polishing with water- based α-alumina powder 0.3 μm and 0.05 μm coarseness (Struers) until mirror finish. To remove any traces of alumina in the surface, the GC was rinsed with milli-Q water before and after sonicating for a couple of minutes in milli-Q water. Finally, the GC was dried with a nitrogen stream to prevent any addition of water to the electrochemical cell during electrodeposition. Before starting any electrochemistry, the DES solution was dried with an Ar stream for a couple of hours to avoid the solvent co-reduction and reduce traces of water in the solvent which may affect the deposition. For all experiments carried out in DES, the cell was kept at 70°C through a water bath circulator to decrease the viscosity of the DES and increases the deposition rate but prevent the co-reduction of the solvent.[52] The electrodeposition process was electrochemically characterized by cyclic voltammetry (CV) from which we have chosen the potential to perform the electrodeposition. Subsequently, the Cu-Ag nanostructures were prepared by applying a constant potential by chronoamperometry (CA) until reaching the chosen circulated charges (i.e. the deposit loading on the GC). For each bath composition, we have deposited four different circulated charges: -7.5 mC, -10 mC, -18 mC and -25 mC. Due to the high similarity of the deposit at -7.5 mC and -10mC, the characterization of the samples at -7.5 mC are only shown in the Supporting Information (S.I.). Once the Cu-Ag nanostructures were deposited, we have only cleaned the surface with hot milli-Q water to remove any traces of the DES as it

is soluble in water.[27] A Bio-Logic potentiostat was used for measurements and analysis of the data.

The morphological analysis was performed in two different scanning electron microscopes (SEM). A JEOL 7800-F prime SEM at the Niels Bohr Institute at the University of Copenhagen and a high-resolution Zeiss Gemini 500 field-emission scanning electron microscope (FE-SEM) at Topsoe S/A. The images were acquired in both cases with a beam energy of 2 kV. A higher beam energy of 15 kV was used for the compositional analysis of the energy dispersive X-ray (EDS) spectroscopy analysis. The EDS data was collected with a Thermo Scientific UltraDry silicon drift detector with Pathfinder Software at Tospoe S/A.

The surface compositional analysis was carried out by X-ray photoelectron spectroscopy (XPS) from the Technical University of Denmark (DTU). A Theta Probe instrument (Thermo Qouite Scientific) was used with an Al anode X-ray source (K$\alpha$ line = 1486.6 eV) and a chamber's base pressure lower than $5.0 \times 10^{-8}$ mbar. The beam size was 400 $\mu$m and the pass energy 100 eV. 4We measured the surveys and elements spectra before and after sputtering for 20 seconds (4 kV and 1.0 $\mu$A) with N6 Ar ($1.1 \times 10^{-7}$ mbar). First, an average of 20 scans was recorded for the surveys followed by 50 scans of each element spectrum in steps of 0.1 eV. We recorded the spectra of C1$s$, O1$s$, Cu2$p$ and Ag3$d$ peaks in all cases. The software for the acquisition and analysis of the data was Thermo Avantage. A Shirley type background was applied for all instances and all peaks were fitted with a Gaussian-Lorentzian mix GL(100) line shape with full width half maximum (FWHM) below 3.5 eV.

The Pb UPD experiments for the estimation of the ECSA and R were performed in a conventional three-electrode glass cell through voltametric analysis using the Bio-Logic potentiostat. UPD is a reversible surface process which is sensitive to both the structure and active area of the catalysts. Previous works have probed the use of UPD for the characterization of silver and copper surfaces among other metals.[61,62] The counter electrode was a Pt wire,

and the reference electrode was a calomel electrode (SCE) from Crison placed on a Luggin capillary. The working electrode were the prepared Cu-Ag nanostructures on GC. We employed a solution of 2 mM $Pb(ClO_4)_2$ (Sigma-Aldrich, $\geq$ 99.995%) + 0.1 M $KClO_4$ (Sigma-Aldrich, $\geq$ 99.99%) + 1 mM $HClO_4$ (suprapur 70%, Merck) in milli-Q water to carry out the lead UPD experiments. After recording the voltammograms, and average of the integrated charges from the anodic and the cathodic scan was calculated. Those values were then used to determine the ECSA and R of our nanostructures using the following equation:

$$ECSA = Q \ (\mu C) \ / \ Q_o^{Cu,Ag}(\mu C \ cm^{-2}) \tag{1}$$

$$R = A_{ECSA} \ (cm^2) \ / \ A_{GEO} \ (cm^2) \tag{2}$$

Where Q is the average integrated charge, $Q_o^{Cu,Ag}$ is the average of the surface charge density values of the lead UPD on polycrystalline extended Cu and Ag surfaces, $A_{ECSA}$ is the calculated electrochemically active surface area and $A_{GEO}$ is the geometric area of our electrode.

## Results and Discussion

We have first electrochemically characterized the co-electrodeposition process of Ag and Cu from a 0.075 M $CuCl_2$: 0.025 M AgCl + DES solution (i.e., from a 3u:1Ag molar ratio solution) by cyclic voltammetry (CV) and chronoamperometry (CA). The voltammograms inform us about the processes happening on the surface at the different swapped potentials, providing the optimal potential range to perform the electrodeposition. Figure 1A shows the recorded voltammograms at different cathodic potentials limits between -0.8 $V_{Ag|AgCl}$ and -1.35 $V_{Ag|AgCl}$. The reversible process of $Cu^{2+}$ to $Cu^{1+}$ appears in all CVs at 0.22 $V_{Ag|AgCl}$ with its oxidation counter-part at 0.43 $V_{Ag|AgCl}$. Following the cathodic scan, we observed an increase in the negative current related with the onset of the electrodeposition at c.a. -0.6 $V_{Ag|AgCl}$. For the shortest potential limit (black line) of -0.8 $V_{Ag|AgCl}$, the reverse scan exhibits a loop

9

(arrows) characteristic of a nucleation and growth mechanism of metallic nanoparticles (NPs), as reported in previous works. First, an overpotential is needed for the formation of stable nuclei due to the weak glassy carbon-metal interaction. Then, the loop appears due to a higher interaction of metal-metal when the formed stable nuclei grow. For the larger cathodic potential limits of -0.95 $V_{Ag|AgCl}$ and -1.35 $V_{Ag|AgCl}$, we only observed a single reduction peak, suggesting that both metals are being electrodeposited at the same time or at similar potential values. In the anodic scan, a first oxidation peak appears around -0.33 $V_{Ag|AgCl}$ which increases in intensity while enlarging the potential limit. At the longest potential limits, these peaks overlap with a new broad peak that appears at slightly more negative potentials. These peaks are related with the oxidation of $Cu^0$ to $Cu^{1+}$ since copper oxidizes prior to silver. The second main oxidation peak between -0.24 V and 0.0 $V_{Ag|AgCl}$ corresponds to Ag and/or Cu-Ag oxidation. The CVs recorded at larger potential limits present a more intense oxidation peak since more metals have been electrodeposited and subsequently oxidized. After recording the cyclic voltammograms to address the potential region where Cu and Ag co-deposits, we have recorded the CA transients aiming to find the most suitable potentials to perform the co-electrodeposition of the metals on the glassy carbon (GC). Figure 1B shows the recorded j-t transients at the different applied potentials. All curves display the characteristic nucleation and growth shape with a potential-dependent current maximum at a certain time which then decays and overlaps at longer times. When the current decays, the mechanism is not potential-dependent anymore but diffusion-controlled. As the applied potential increases, the maximum current peak is attained at lower times suggesting faster nucleation and growth. We only observed a single maximum on all the recorded j-t transients, corroborating the co-electrodeposition of the metals together.
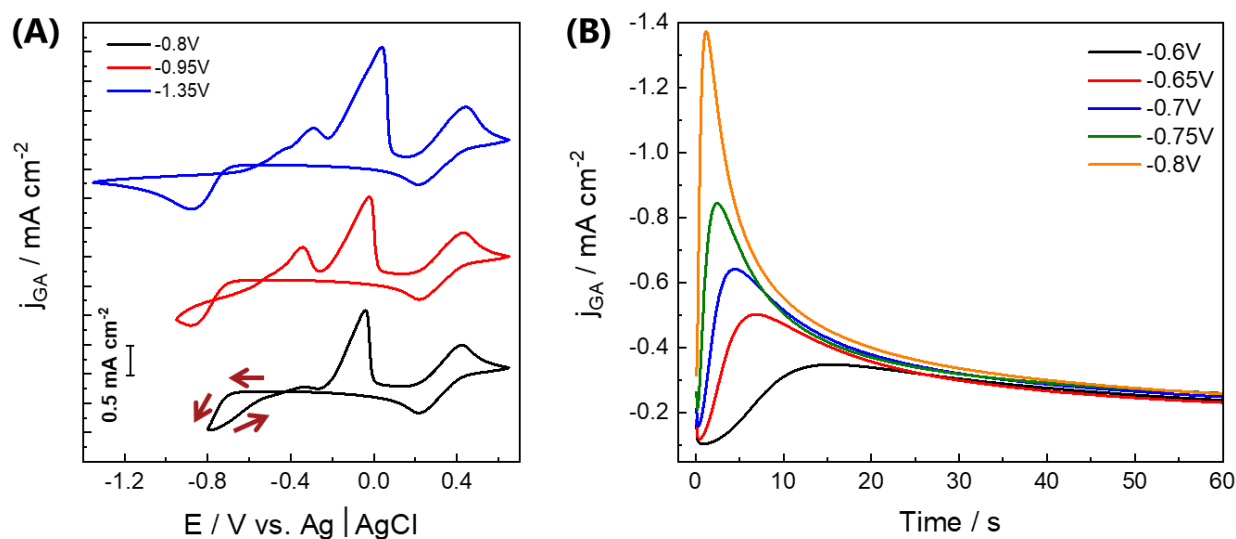
10

**Figure 1.** Electrochemical characterization of the electrodeposition process from a 0.075 M $CuCl_2$: 0.025 M AgCl + DES solution (3Cu:1Ag) by **(A)** voltammetric analysis at different cathodic potential limits and **(B)** j-t transients at different applied potentials. Scan rate: 50 mV/s.

To prepare the deposits, we have selected moderate applied potentials between -0.65 V and -0.75 V at which the nucleation and growth mechanism does not happen to slow nor too fast as seen in the CAs. The selection of these potential values aims to avoid a poorly adherent deposit or an uncontrollable deposition mechanism with dendritic growth that occurs if the deposition takes place too slow or too fast respectively. Additionally, we have prepared four different coverages by controlling the time of deposition and circulated charge until reaching -7.5 mC, -10 mC, -18 mC and -25 mC. This way, we analyse how the coverage influence the size, morphology, and composition of the nanostructures at the different applied potentials. Due to the similarities of the sample at -7.5 mC and -10 mC, all measurements and characterization of the samples at -7.5 mC appears in the supporting information (S.I.).

Figure 2 shows the SEM images of the prepared nanostructures from the 3Cu:1Ag bath solution at different applied potentials and circulated charges. All the nanostructures have formed NPs homogeneously distributed over the whole GC surface. Figure 2A, 2B and 2C show the

11

nanostructures prepared at -0.65 $V_{Ag|AgCl}$ and -10 mC, -18 mC and -25 mC, respectively. From visual inspection from SEM, we precipitated rounded NPs with pores. Some tiny spikes are occasionally observed on top of a few NPs for the samples at -18 mC. However, these spikes are not stable at -0.65 $V_{Ag|AgCl}$ and completely disappear for the -25 mC deposit. The size of the NPs increases with the loading from 200 nm at -10 mC up to 500 nm at -25 mC. On the other hand, when preparing the deposits at the faster deposition rate of -0.75 $V_{Ag|AgCl}$ (Figure 2D, 2E and 2F), the NPs does not notably increase in size with the coverage, but tiny spikes appear on top of the rounded and porous NPs of 200-300 nm. The spikes are observable in all the samples at this applied potential being more notorious for the sample at -25 mC. In addition, we notice a clear increase in the coverage of the NPs over the GC surface while increasing the circulated charge from -10 mC to -18 mC and to -25 mC. These observations show that we can tune the size and morphology of Cu-Ag nanostructures by simply adjusting the circulated charge and applied potential.
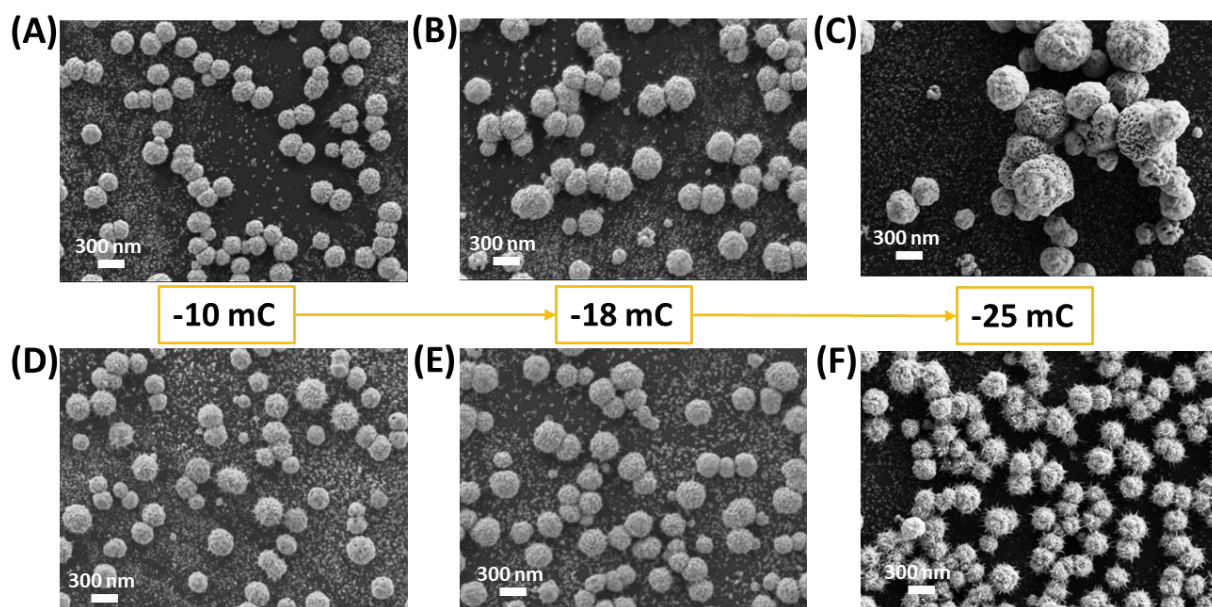


Figure 2. SEM images of the 3Cu:1Ag nanostructures at (A-C) -0.65 $V_{Ag|AgCl}$ and (D-F) -0.75 $V_{Ag|AgCl}$. Each potential at circulated charges of -10mC, -18 mC and -25mC from left to right.

After the SEM analysis, we have analysed the composition of the 3Cu:1Ag nanostructures by EDS. Figure 3 shows the EDS colour maps of the 3Cu:1Ag samples at -18 mC. We have verified that Cu and Ag together are homogeneously distributed over the glassy carbon substrate in both cases. The semi-quantitative EDS analysis of the sample prepared at the lower potential of -0.65 $V_{Ag|AgCl}$ indicates a Cu and Ag mass relation of 1.8:1. Similarly, the sample at -0.75 $V_{Ag|AgCl}$ has only a slightly lower Cu and Ag relationship of 1.6:1.



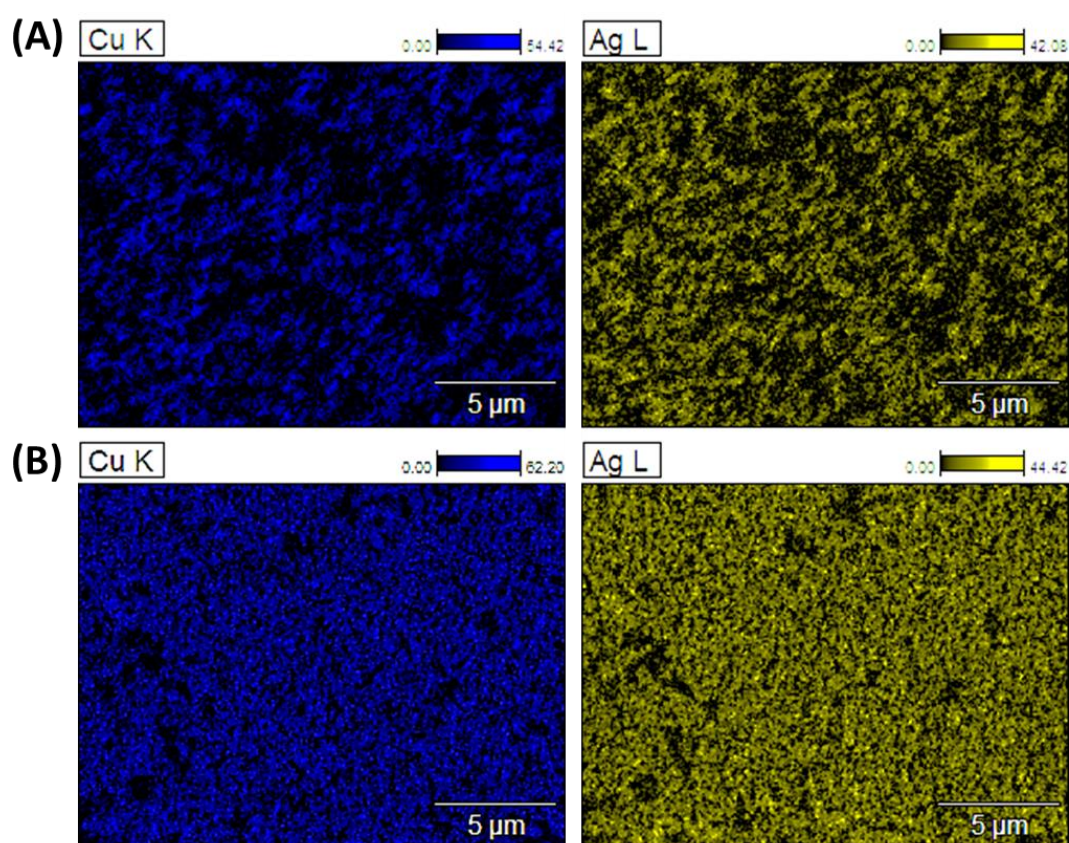**Figure 3.** EDS colour maps analysis of the 3Cu:1Ag samples at -18 mC and (A) -0.65 $V_{Ag|AgCl}$, and (B) -0.75 $V_{Ag|AgCl}$. Blue maps correspond to copper and yellow maps correspond to silver.

With the aim of assessing how the bath composition affects the size, shape, and composition of the nanostructures, we have characterized two Cu-Ag systems from bath solutions of 1Cu:1Ag and 6Cu:1Ag molar ratio solutions. The electrochemical characterization is shown in Figure S1. In both cases, we have found a single reduction peak starting at the same potential than for the 3Cu:1Ag molar ratio solution. The CV of the 1Cu:1Ag solution in Figure S1A,

shows that the first Cu oxidation peaks on the anodic scan mainly disappear while the second oxidation peak increases in intensity (Fig. S1A). When enlarging the potential limit (blue line), this Cu oxidation peak can be better identified. These observations suggest that Ag is probably electrodeposited at less negative potentials than Cu as it can be inferred from the studies of single Cu and single Ag in the literature.[52,53,57] These studies show that the onset potential for the Cu electrodeposition is at c.a. -0.8 $V_{Ag|AgCl}$ whereas we have shown the electrochemical characterization for single Ag electrodeposition in the S.I. with the onset potential located at c.a. -0.3 $V_{Ag|AgCl}$. Consequently, the kinetics of the silver electrodeposition becomes faster, leading to less copper and more silver being electrodeposited in accordance with the increase of silver in the bath solution. Figure S1C shows the CV for the 6Cu:1Ag bath solution. In contrast to the 1Cu:1Ag, the first Cu oxidation peak has overlapped with the second oxidation peak and become broader. At the largest potential limit, a set of broad and lower peaks between -0.5 $V_{Ag|AgCl}$ and -0.24 $V_{Ag|AgCl}$ overlap with the main oxidation peaks. All these peaks are likely related with the oxidation of both Cu and Ag, suggesting that more copper is being electrodeposited and subsequently oxidized in the reverse scan. In addition, the increase in intensity of the $Cu^{1+}$ to $Cu^{2+}$ peak also suggests an increase of the amount of deposited copper. Figure S1B and S1D show the CA curves of the 1Cu:1Ag and 6Cu:1Ag with the characteristic shape of the nucleation and growth mechanism with a single potential-dependant current maximum peak.

Following the same analysis than for the 3Cu:1Ag nanostructures, we have prepared 1Cu:1Ag and 6Cu:1Ag deposits at two applied potentials and at four circulated charges. Figure 4A and 4B show the SEM images of the -18 mC 1Cu:1Ag nanostructures at -0.65 $V_{Ag|AgCl}$ and -0.75 $V_{Ag|AgCl}$, respectively. The NPs exhibit a less rounded (or irregular) and less porous structure than for the 3Cu:1Ag nanostructures. The morphology of the 1Cu:1Ag nanostructure resembles the one shown in Figure S10C from a single silver nanostructure, suggesting a higher

14

contribution of silver in these bimetallic nanostructures. For the same circulated charge, the NPs decreases in size from 500 nm to 300 nm with the applied potential. Even though the formed NPs are bigger at -0.65 $V_{Ag|AgCl}$, the GC is less covered compared to the sample prepared at -0.75 $V_{Ag|AgCl}$. The images for the circulated charges of -7.5 mC, -10 mC and -25 mC are shown in Figure S3 of the S.I. For both applied potentials, the NPs have increased in size with the circulated charge being more notorious for the samples prepared at -0.65 $V_{Ag|AgCl}$. The shape does not significantly change.

Figure 4C and 4D illustrate the SEM images of the -18 mC 6Cu:1Ag nanostructures at -0.68 $V_{Ag|AgCl}$ and -0.73 $V_{Ag|AgCl}$, respectively. They have a similar morphology to the 3Cu:1Ag nanostructures. Figure 4C shows rounded and porous NPs up to 300 nm and with no spikes while figure 4D exhibits the rounded NPs of the same size but seem less porous and have tiny spikes on top of most of them. In contrast to the 3Cu:1Ag nanostructures, these spikes are notably smaller. If we analyse the samples at the other circulated charge in Figure S4, we observe how at -0.73 $V_{Ag|AgCl}$ these spikes are not stable at higher circulated charges and do not appear yet at -7.5 mC. These changes on the spikes appearance suggest that they are not stable when the amount of copper on the bath solution is too high. The size of the 6Cu:1Ag nanostructures does not substantially change at any of the two potentials with the circulated charge. We do not observe coalescence of the particles, which distribute homogenously and cover more areas of the GC surface when the circulated charge increases from -7.5 mC to -25 mC
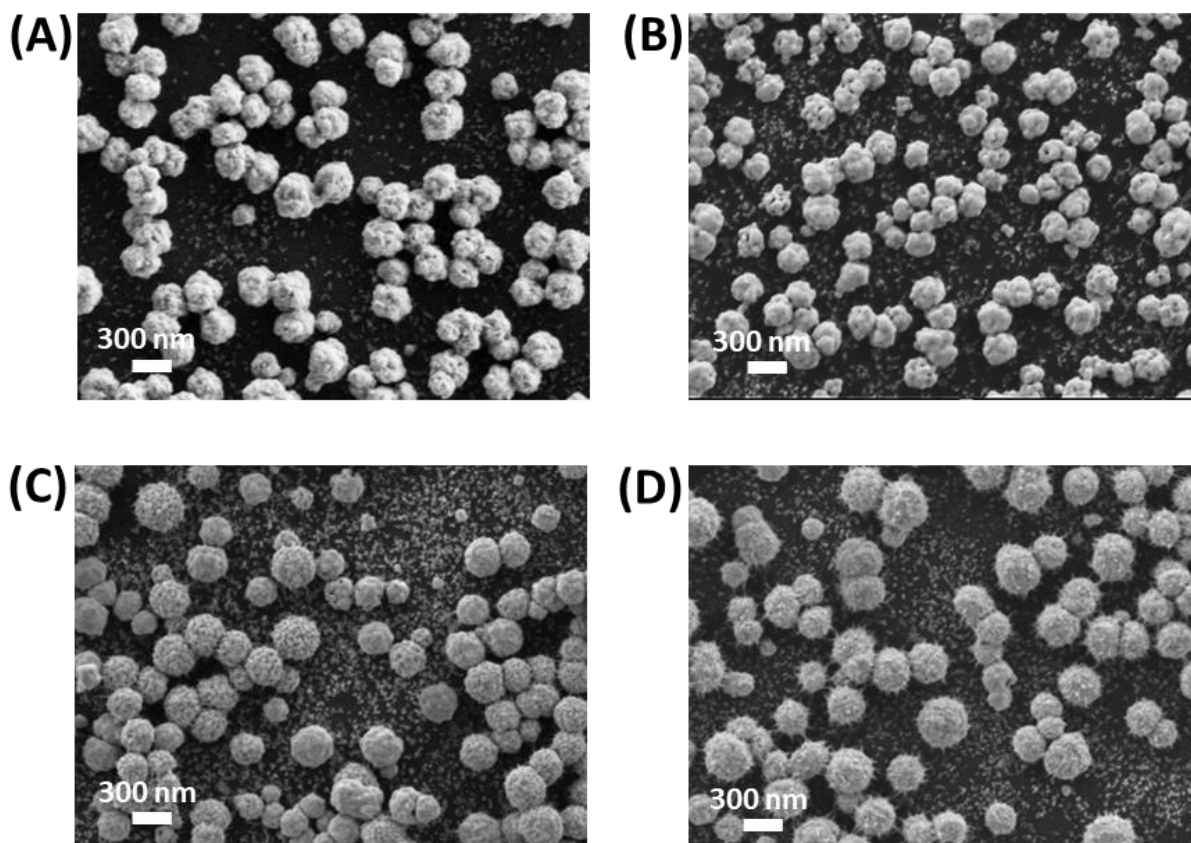
**Figure 4.** SEM images of the 1Cu:1Ag nanostructures at **(A)** -0.65 $V_{Ag|AgCl}$ and at **(B)** -0.75 $V_{Ag|AgCl}$ and, of the 6Cu:1Ag nanostructures at **(C)** -0.68 $V_{Ag|AgCl}$ and at **(D)** -0.73 $V_{Ag|AgCl}$. All samples have a circulated charge of -18 mC.

The EDS analysis of the 1Cu:1Ag and 6Cu:1Ag nanostructures prepare at -18 mC (Figure 4) at -18 mC are shown in Figure S5 and Figure S6 of the S.I. The colour maps have confirmed the presence of Cu and Ag homogeneously distributed over the GC surface. The semi-qualitative mass composition analysis obtained for the 1Cu:1Ag nanostructures at -0.65 $V_{Ag|AgCl}$ and -0.75 $V_{Ag|AgCl}$ are 1: 3.3 and 1: 5.5, respectively. For the 6Cu:1Ag nanostructures at -0.68 $V_{Ag|AgCl}$ and -0.73 $V_{Ag|AgCl}$, the mass relation from the EDS analysis are 4.3: 1 and 2.5: 1, respectively. The composition of the deposited nanostructures does not follow the bath molar ratio of Cu and Ag as Cu and Ag have different deposition kinetics. However, the composition is influenced by it, with a clear increase of either Ag for the 1Cu:1Ag and Cu for

16

the 6Cu:1Ag, showing that we control the Cu/Ag molar ratio in the nanostructures by adjusting the bath composition.

We also performed XPS analysis to investigate the chemical composition and chemical states of the elements on the surface layers because the EDS analysis provides information about the bulk composition. The spectra of the nanostructures at -18 mC have been recorded after 20 seconds of sputtering to remove the first surface layers in order to avoid any traces of contamination. Figure 5A, 5B and 5C show the Cu$2p$ and Ag$3d$ peaks from the XPS spectra of the 3Cu:Ag, 1Cu:1Ag and 6Cu:1Ag nanostructures at the faster electrodeposition applied potentials (-0.75 V$_{Ag|AgCl}$, -0.75 V$_{Ag|AgCl}$ and -0.75 V$_{Ag|AgCl}$, respectively). The surveys before and after sputtering are also illustrated in Figure S7 of the S.I. The Cu$2p$ region presents split spin-orbit components identified as Cu$2p_{1/2}$ and Cu$2p_{3/2}$ with an energy separation of 20 eV. To identify the chemical states of copper, the spectra present characteristic satellites features. All samples from Figure 5 show the weak satellite features at c.a. 945 eV which are related with the oxidation state of Cu$^{1+}$. In contrast to Cu$^{2+}$, neither Cu$^0$ and Cu$^{1+}$ present the pronounce double satellite peak found at c.a. 943 eV. This oxidation state is in good agreement with the binding energies of the two Cu$2p_{3/2}$ components from our fitting at c.a. 933 eV. Both, metallic copper and Cu$_2$O appear close to this binding energy while CuO usually has the Cu$2p$ peaks broader and shifted to higher binding energies.[63–65] The right panels of Figure 5 show the main Ag$3d$ region which also exhibit well-separated split spin-orbit components: Ag$3d_{3/2}$ and Ag$3d_{5/2}$. The metallic silver is located at a binding energy of 368.2 eV, close to the value of 368.5 eV we have obtained from the fitting of our nanostructures. Metallic silver is often accompanied by characteristic weak loss features at higher binding energies of each component, where silver presents plasmon losses, as indicated in Figure 5A with arrows. These specific energy losses on metallic silver appear when the photoelectrons interact with other

electrons. The applied Shirley background has not subtracted these specific losses since it only assumes a constant energy loss function due to the inelastic scattering events.[66,67]
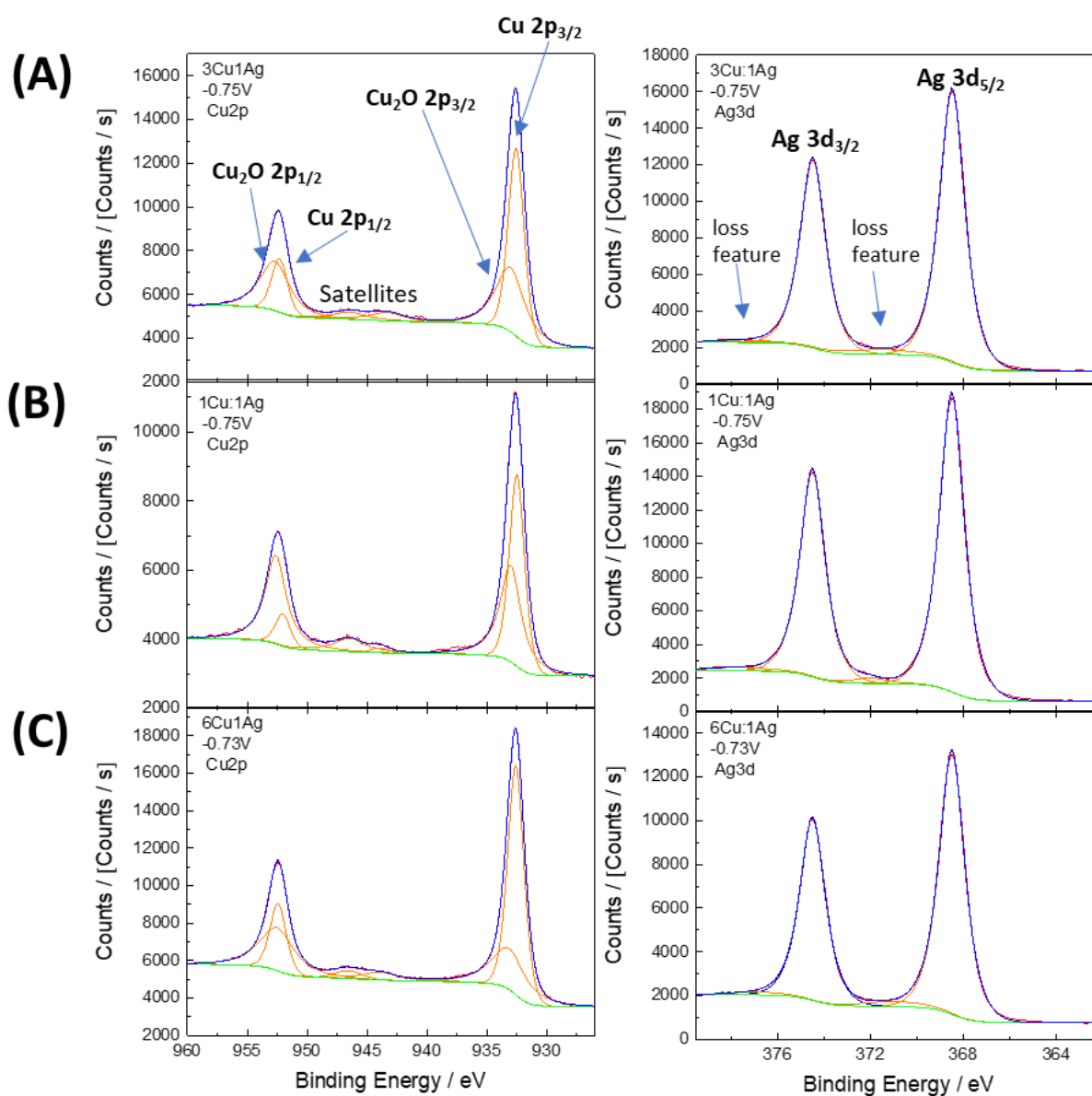


**Figure 5.** XPS analysis of Cu*2p* and Ag*3d* peaks of the **(A)** 3Cu:1Ag at -0.75 $V_{Ag|AgCl}$, **(B)** 1Cu:1Ag -0.75 $V_{Ag|AgCl}$ and **(C)** 6Cu:1Ag at -0.73 $V_{Ag|AgCl}$ nanostructures with a circulated charge of -18 mC at each level 1: 20s surface etching.

From the Cu*2p* and Ag*3d* peaks intensity, we have observed that the Cu*2p* intensities increase while the Ag*3d* intensities decrease following the order of 1Cu:1Ag, 3Cu:1Ag and 6Cu:1Ag bath solutions. We have estimated a surface Cu:Ag atomic relation of 1.1: 1 from 3Cu:1Ag

(Fig. 5A), 1: 1.6 from 1Cu:1Ag (Fig. 5B) and 1.7: 1 from 6Cu:1Ag (Fig. 5C) for the samples prepared at -18 mC. The amount of Cu and Ag in the surface layers of our nanostructures are closer to 50/50 i.e., they are richer in silver at the surface than at the bulk electrode. We ascribe the differences between the bulk and the surface composition to the fact that the kinetics of the most abundant metal in the bath becomes favourable at the beginning of the electrodeposition while during the growth of the NPs, the metallic nuclei facilitate the electrodeposition of both metals together. The need for more Cu in the bath solution to reach a 50/50 Cu and Ag composition is also attributed to the lower overpotential of the Ag electrodeposition. Nevertheless, more mechanistic studies are necessary to fully understand the different stages of the electrodeposition process. Another plausible explanation for the higher amount of silver in the surface might be the lower surface energy of silver in compared with copper which causes silver to migrate to the surface.[68] Figure S8 shows the XPS analysis of the Cu*2p* and Ag*3d* peaks of the 3Cu:Ag, 1Cu:1Ag and 6Cu:1Ag nanostructures at the slower deposition rates (-0.65 $V_{Ag|AgCl}$, -0.65 $V_{Ag|AgCl}$ and -0.68 $V_{Ag|AgCl}$, respectively). They present the same features as in Figure 5. The estimated surface weight relation of Cu and Ag from the XPS fitting of Figure S8 are 0.9: 1 for the 3Cu:1Ag deposit, 1: 1.9 for the 1Cu:1Ag deposit and 1.7: 1 for the 6Cu:1Ag deposit. These values are similar to the ones from Figure 5. Only small variations are observed. When the deposition rate is slower and there is less copper in the bath, the deposition kinetics of silver might be slightly more favourable, due to the lower applied potential for electrodeposition. Nevertheless, the differences in composition varies little with the applied potential conditions and could be more related to a more surface effect if the GC has small irregularities originated from the mechanical polishing. It is important to mention that both the EDS and XPS analysis are carried out ex-situ, meaning that the surface composition can change with respect to the bulk composition when the sample are brought to open circuit potential or exposed to air.
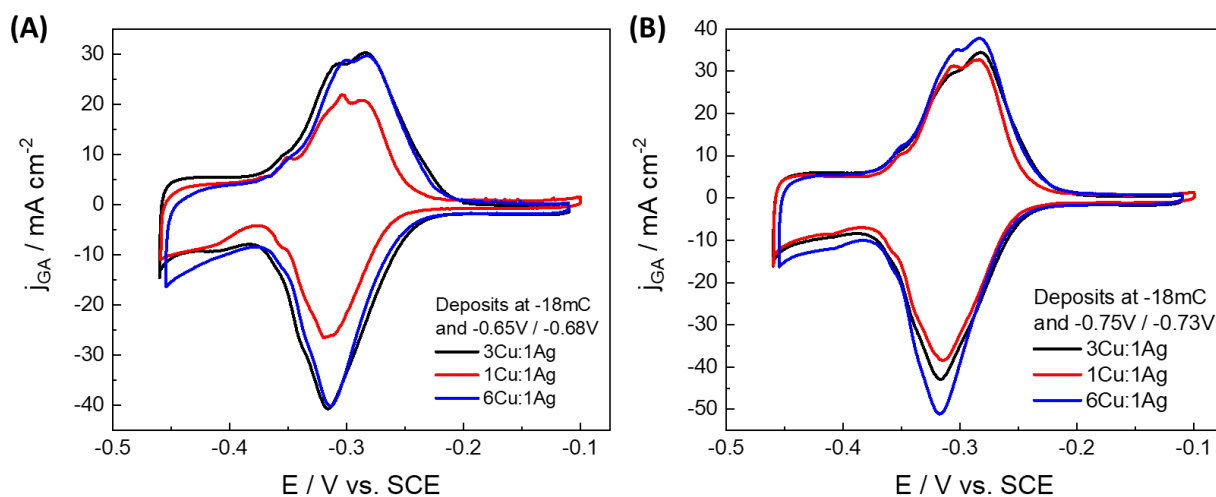
**Figure 6.** Pb UPD of the Cu-Ag nanostructures at (A) -0.65 $V_{Ag|AgCl}$ for 3Cu:1Ag and 1Cu:1Ag and -0.68 $V_{Ag|AgCl}$ for 6Cu:1Ag and, (B) -0.75 $V_{Ag|AgCl}$ for 3Cu:1Ag and 1Cu:1Ag and -0.73 $V_{Ag|AgCl}$ for 6Cu:1Ag. The black lines correspond to the 3Cu:1Ag, red lines to the 1Cu:1Ag and blue lines to the 6Cu:1Ag nanostructures at -18 mC. Scan rate: 5 mV s$^{-1}$.

After the characterization of the Cu-Ag nanostructures, we have conducted lead underpotential deposition (UPD) to assess the electrochemically active surface area (ECSA) and roughness factor (R) of the deposited samples. The ECSA is an important parameter in electrocatalysis because it allows to address the intrinsic activity of the NPs and gives key information to elucidate the structure-property relationships. Figure 6 shows the voltametric responses of our Cu-Ag nanostructures at -18 mC for the studied applied potentials. The voltammograms show similar groups of features which are quasi-reversible. In Figure 6A, we have identified one broad peak in the anodic scans centred at c.a. -0.30 $V_{SCE}$ Its counterpart in the cathodic scans is broader with a main peak centred at c.a. -0.31 $V_{SCE}$. Figure 6B also exhibits one intense and broad anodic peak for the three samples, which is centred at the same potentials as the samples from Figure 6A. Another important aspect that we have noticed is the decrease in intensity of the samples of 1Cu:1Ag, especially for the samples prepared at -0.65 $V_{Ag|AgCl}$. We ascribe the decrease in current of the 1Cu:1Ag sample to the fact that the deposits with more silver are less

adherent and easily get detached during the UPD measurements or after carrying out electrochemistry on them. The SEM and UPD analysis of silver electrodeposition on GC in Figure S10 have confirmed the poor adherence of silver on GC due to a high surface diffusion (more detailed explanation in the S.I.).

**Table 1.** Summary of the estimated ECSA (mA cm$^{-2}$) and R from the Pb UPD analysis.

| Bath composition | Applied E | ECSA / mA cm$^{-2}$ | | | Roughness factor (R) | | |
|---|---|---|---|---|---|---|---|
| | | -10mC | -18mC | -25mC | -10mC | -18mC | -25mC |
| 1Cu:1Ag | -0.55V | 0.18 | 0.18 | 0.29 | 0.61 ± 0.01 | 0.91 ± 0.03 | 1.41 ± 0.08 |
| | -0.65V | 0.19 | 0.27 | 0.36 | 0.98 ± 0.04 | 1.41 ± 0.06 | 1.87 ± 0.04 |
| 3Cu:1Ag | -0.55V | 0.22 | 0.29 | 0.31 | 1.03 ± 0.07 | 1.47 ± 0.06 | 1.71 ± 0.1 |
| | -0.65V | 0.21 | 0.30 | 0.37 | 1.12 ± 0.06 | 1.52 ± 0.01 | 1.96 ± 0.08 |
| 6Cu:1Ag | -0.6V | 0.22 | 0.27 | 0.33 | 1.13 ± 0.08 | 1.39 ± 0.04 | 1.69 ± 0.05 |
| | -0.65V | 0.22 | 0.31 | 0.36 | 1.13 ± 0.01 | 1.57 ± 0.01 | 1.82 ± 0.05 |

By integrating the charge under the cathodic and anodic curves, we estimate the ECSA of the deposits (µC cm$^{-2}$) as explained in the experimental section. To calculate the ECSA, we divide the integrated charges by the surface charge density values of the lead UPD on polycrystalline extended Cu and Ag surfaces which are reported in the literature.[61,62,69] The Pb UPD of the other Cu-Ag nanostructures at -7.5 mC, -10 mc and -25 mC are shown in Figure S9 of the S.I. Table 1 summarizes the ECSA and R of all the Cu-Ag nanostructures of this work. We have obtained R up to 2 and particles of similar size and homogenously distributed. However, we could not prepare surfaces with higher R due to the low adherence of the deposit. The ECSA and R increase with the circulated charge and applied potential.

**Conclusions**

We described, in detail, the preparation of Cu-Ag nanostructures by metal electrodeposition from a choline chloride plus urea DES. The morphological and compositional analysis by SEM, EDS and XPS confirmed the formation of Cu-Ag NPs homogeneously distributed over the surface. The silver-rich deposits formed irregular NPs with lower porosity whereas the samples richer in copper formed rounded and porous nanostructures with tiny spikes, and the particles were more homogeneously distributed on the surface. In both cases, we observed that the surface composition was richer in silver than the bulk composition, and the concentration of copper increased by raising the concentration of copper in the bath solution. We show that the molar Cu/Ag ratio can be tailored by adjusting bath composition and applied potential conditions. Finally, we have determined the ECSA and roughness factor of the samples using lead UPD. Under electrochemical conditions, we have noticed that silver-rich deposits have low adherence, suggesting that a minimum amount of copper is required to obtain stable and homogeneous nanostructures. We have shown that this method allows to prepare Cu-Ag bimetallic nanostructures with tunable size, morphology and composition tailoring the different experimental parameters. Future works should focus on addressing the first stages of the nucleation and growth mechanism. We also highlight that future studies should focus on evaluating the use of other substrates such as metallic substrates and their effect on the active area and stability of the deposits.

ORCID

Paula Sebastián-Pascual: 0000-0001-7985-0750

María Escudero-Escribano: 0000-0002-6432-3015

Elena Plaza-Mayoral: 0000-0001-7208-7940

Kim Nicole Dalby: https://orcid.org/0000-0001-6048-3583

Hanne Falsig: 0000-0002-2474-4093

Ib Chorkendorff: 0000-0003-2738-0325

**Notes**

The authors declare no competing financial interest.

ASSOCIATED CONTENT

A detailed electrochemical characterization of the 1Cu:1Ag and 6Cu:1Ag electrodeposition from DES by CV and CA analysis is included. Additional ex-situ characterization of the Cu-Ag nanostructures with SEM images, EDS, and XPS analysis are added. Finally, lead UPD voltammograms of the Cu-Ag nanostructures for all circulated charges and applied potentials have been represented and further analyzed. The analysis of the single silver electrodeposition with its morphological characterization by SEM and the Pb-UPD voltammetry is added.

Author contribution:

Elena Plaza-Mayoral: Investigation, Conceptualization, Methodology, Formal Analysis, Data curation, Writing - Original Draft, Visualization.

Paula Sebastián:  Supervision, Methodology, Conceptualization, Writing - Original Draft, Visualization, Project Administration.

Kim Nicole Dalby: Ex-situ characterization, Investigation, Formal Analysis, Data Curation, Writing - Review & Editing.

Hanne Falsig: Resources, Writing - Review & Editing.

Ib Chorkendorff: Data curation, Resources, Writing - Review & Editing.

María Escudero Escribano: Supervision, Methodology, Conceptualization, Writing - Review & Editing, Project Administration, Funding Acquisition.

# References

[1]     S. Chu, Y. Cui, N. Liu, The path towards sustainable energy, Nat Mater 16 (2016) 16–22. https://doi.org/10.1038/nmat4834.

[2]     R. Eisenberg, H.B. Gray, G.W. Crabtree, Addressing the challenge of carbon-free energy, Proc Natl Acad Sci U S A 117 (2020) 12543–12549. https://doi.org/10.1073/pnas.1821674116.

[3]     P. De Luna, C. Hahn, D. Higgins, S.A. Jaffer, T.F. Jaramillo, E.H. Sargent, What would it take for renewably powered electrosynthesis to displace petrochemical processes?, Science (1979) 364 (2019). https://doi.org/10.1126/science.aav3506.

[4]     P. Trogadas, V. Ramani, P. Strasser, T.F. Fuller, M.-O. Coppens, Hierarchically Structured Nanomaterials for Electrochemical Energy Conversion, Angewandte Chemie International Edition 55 (2016) 122–148. https://doi.org/https://doi.org/10.1002/anie.201506394.

[5]     G.R. Li, H. Xu, X.F. Lu, J.X. Feng, Y.X. Tong, C.Y. Su, Electrochemical synthesis of nanostructured materials for electrochemical energy conversion and storage, Nanoscale 5 (2013) 4056–4069. https://doi.org/10.1039/c3nr00607g.

[6]     P. Sebastián-Pascual, I. Jordão Pereira, M. Escudero-Escribano, Tailored electrocatalysts by controlled electrochemical deposition and surface nanostructuring, Chemical Communications 56 (2020) 13261–13272. https://doi.org/10.1039/d0cc06099b.

[7]     H. Mistry, A.S. Varela, S. Kühl, P. Strasser, B.R. Cuenya, Nanostructured electrocatalysts with tunable activity and selectivity, Nat Rev Mater 1 (2016). https://doi.org/10.1038/natrevmats.2016.9.

[8]     C.L. Bentley, M. Kang, P.R. Unwin, Nanoscale Surface Structure–Activity in Electrochemistry and Electrocatalysis, J Am Chem Soc 141 (2019) 2179–2193. https://doi.org/10.1021/jacs.8b09828.

[9]     M.T.M. Koper, Structure sensitivity and nanoscale effects in electrocatalysis, Nanoscale 3 (2011) 2054–2073. https://doi.org/10.1039/c0nr00857e.

[10]    T.S. Rodrigues, A.G.M. Da Silva, P.H.C. Camargo, Nanocatalysis by noble metal nanoparticles: Controlled synthesis for the optimization and understanding of activities, J Mater Chem A Mater 7 (2019) 5857–5874. https://doi.org/10.1039/c9ta00074g.

[11]    N. Tian, B.-A. Lu, X.-D. Yang, R. Huang, Y.-X. Jiang, Z.-Y. Zhou, S.-G. Sun, Rational Design and Synthesis of Low-Temperature Fuel Cell Electrocatalysts, Electrochemical Energy Reviews 1 (2018) 54–83. https://doi.org/10.1007/s41918-018-0004-1.

[12]    Z.-P. Wu, S. Shan, S.-Q. Zang, C.-J. Zhong, Dynamic Core–Shell and Alloy Structures of Multimetallic Nanomaterials and Their Catalytic Synergies, Acc Chem Res (2020). https://doi.org/10.1021/acs.accounts.0c00564.

[13]    M. Escudero-Escribano, P. Malacrida, M.H. Hansen, U.G. Vej-Hansen, A. Velazquez-Palenzuela, V. Tripkovic, J. Schiøtz, J. Rossmeisl, I.E.L. Stephens, I. Chorkendorff, Tuning the activity of Pt alloy electrocatalysts by means of the lanthanide contraction, Science (1979) 352 (2016) 73–76. https://doi.org/10.1126/science.aad8892.

[14]    J. Li, H. Xiong, X. Liu, D. Wu, D. Su, B. Xu, Q. Lu, Weak CO binding sites induced by Cu–Ag interfaces promote CO electroreduction to multi-carbon liquid products, Nat Commun 14 (2023). https://doi.org/10.1038/s41467-023-36411-5.

[15]    L. Wang, D.C. Higgins, Y. Ji, C.G. Morales-Guio, K. Chan, C. Hahn, T.F. Jaramillo, Selective reduction of CO to acetaldehyde with CuAg electrocatalysts, 117 (2020) 12572–12575. https://doi.org/10.1073/pnas.1821683117/-/DCSupplemental.

[16]    E.L. Clark, C. Hahn, T.F. Jaramillo, A.T. Bell, Electrochemical CO2 Reduction over Compressively Strained CuAg Surface Alloys with Enhanced Multi-Carbon Oxygenate Selectivity, J Am Chem Soc 139 (2017) 15848–15857. https://doi.org/10.1021/jacs.7b08607.

[17]    Y. Qiao, G. Kastlunger, R.C. Davis, C.A.G. Rodriguez, A. Vishart, W. Deng, Q. Xu, S. Li, P. Benedek, J. Chen, J. Schröder, J. Perryman, D.U. Lee, T.F. Jaramillo, I. Chorkendorff, B. Seger, Mechanistic Insights into Aldehyde Production from Electrochemical CO 2 Reduction on CuAg Alloy via Operando X-ray Measurements , ACS Catal (2023) 9379–9391. https://doi.org/10.1021/acscatal.3c01009.

[18]    P. Iyengar, M.J. Kolb, J.R. Pankhurst, F. Calle-Vallejo, R. Buonsanti, Elucidating the Facet-Dependent Selectivity for CO2Electroreduction to Ethanol of Cu-Ag Tandem Catalysts, ACS Catal 11 (2021) 4456–4463. https://doi.org/10.1021/acscatal.1c00420.

[19]    D. Higgins, M. Wette, B.M. Gibbons, S. Siahrostami, C. Hahn, M. Escudero-Escribano, M. García-Melchor, Z. Ulissi, R.C. Davis, A. Mehta, B.M. Clemens, J.K. Nørskov, T.F. Jaramillo, Copper Silver Thin Films with Metastable Miscibility for Oxygen Reduction Electrocatalysis in Alkaline Electrolytes, ACS Appl Energy Mater 1 (2018) 1990–1999. https://doi.org/10.1021/acsaem.8b00090.

[20]    K.H. Lee, W. Kong, M. Han, D.J. Park, J.H. Ahn, S.Z. Han, Y.B. Park, K.H. Lee, S. Choe, Properties of nanocrystalline CuAg foil prepared via electrodeposition, J Alloys Compd 881 (2021). https://doi.org/10.1016/j.jallcom.2021.160522.

[21]    M.J. Kim, K.J. Park, T. Lim, O.J. Kwon, J.J. Kim, Fabrication of Cu-Ag Interconnection Using Electrodeposition: The Mechanism of Superfilling and the Properties of Cu-Ag Film, J Electrochem Soc 160 (2013) D3126–D3133. https://doi.org/10.1149/2.020312jes.

[22]    J. Hsieh, S. Hung, The effect of cu: Ag atomic ratio on the properties of sputtered cu-ag alloy thin films, Materials 9 (2016). https://doi.org/10.3390/ma9110914.

[23]    J.D. Lee, J.B. Miller, A. V. Shneidman, L. Sun, J.F. Weaver, J. Aizenberg, J. Biener, J.A. Boscoboinik, A.C. Foucher, A.I. Frenkel, J.E.S. Van Der Hoeven, B. Kozinsky, N. Marcella, M.M. Montemore, H.T. Ngan, C.R. O'Connor, C.J. Owen, D.J. Stacchiola, E.A. Stach, R.J. Madix, P. Sautet, C.M. Friend, Dilute Alloys Based on Au, Ag, or Cu for Efficient Catalysis: From Synthesis to Active Sites, Chem Rev (2021). https://doi.org/10.1021/acs.chemrev.1c00967.

[24]    M.T. Nguyen, T. Yonezawa, Sputtering onto a liquid: interesting physical preparation method for multi-metallic nanoparticles, Sci Technol Adv Mater 19 (2018) 883–898. https://doi.org/10.1080/14686996.2018.1542926.

[25]    D. Li, C. Wang, D. Tripkovic, S. Sun, N.M. Markovic, V.R. Stamenkovic, Surfactant removal for colloidal nanoparticles from solution synthesis: The effect on catalytic performance, ACS Catal 2 (2012) 1358–1362. https://doi.org/10.1021/cs300219j.

[26]    L. García-Cruz, V. Montiel, J. Solla-Gullón, Shape-controlled metal nanoparticles for electrocatalytic applications, Physical Sciences Reviews 4 (2018) 20170124. https://doi.org/https://doi.org/10.1515/psr-2017-0124.

[27]    Q. Zhang, K. De Oliveira Vigier, S. Royer, F. Jérôme, Deep eutectic solvents: Syntheses, properties and applications, Chem Soc Rev 41 (2012) 7108–7146. https://doi.org/10.1039/c2cs35178a.

[28]    R. Bernasconi, G. Panzeri, A. Accogli, F. Liberale, L. Nobili, L. Magagnin, Electrodeposition from Deep Eutectic Solvents, Progress and Developments in Ionic Liquids (2017). https://doi.org/10.5772/64935.

[29]    L.I.N. Tomé, V. Baião, W. da Silva, C.M.A. Brett, Deep eutectic solvents for the production and application of new materials, Appl Mater Today 10 (2018) 30–50. https://doi.org/10.1016/j.apmt.2017.11.005.

[30]    E.L. Smith, A.P. Abbott, K.S. Ryder, Deep Eutectic Solvents (DESs) and Their Applications, Chem Rev 114 (2014) 11060–11082. https://doi.org/10.1021/cr300162p.

[31]    A.P. Abbott, D. Boothby, G. Capper, D.L. Davies, R.K. Rasheed, Deep Eutectic Solvents Formed between Choline Chloride and Carboxylic Acids:  Versatile Alternatives to Ionic Liquids, J Am Chem Soc 126 (2004) 9142–9147. https://doi.org/10.1021/ja048266j.

[32]    D. V. Wagle, H. Zhao, G.A. Baker, Deep eutectic solvents: Sustainable media for nanoscale and functional materials, Acc Chem Res 47 (2014) 2299–2308. https://doi.org/10.1021/ar5000488.

[33]    C. Li, M. Iqbal, J. Lin, X. Luo, B. Jiang, V. Malgras, K.C.W. Wu, J. Kim, Y. Yamauchi, Electrochemical Deposition: An Advanced Approach for Templated Synthesis of Nanoporous Metal Architectures, Acc Chem Res 51 (2018) 1764–1773. https://doi.org/10.1021/acs.accounts.8b00119.

[34]    V. S. Protsenko, F.I. Danilov, Current Trends in Electrodeposition of Electrocatalytic Coatings, in: A.A. Inamuddin, Boddula R. (Ed.), Methods for Electrocatalysis. Springer, Chams, 2020.

[35]    P. Sebastiá, V. Climent, J.M. Feliu, Ionic Liquids in the Field of Metal Electrodeposition, 2018.

[36]    P. Sebastián, L.E. Botello, E. Vallés, E. Gómez, M. Palomar-Pardavé, B.R. Scharifker, J. Mostany, Three-dimensional nucleation with diffusion controlled growth: A comparative study of electrochemical phase formation from aqueous and deep eutectic solvents, Journal of Electroanalytical Chemistry 793 (2017) 119–125. https://doi.org/10.1016/j.jelechem.2016.12.014.

[37]    H.J. Lee, M.J. Kim, T. Lim, K.J. Park, J.J. Kim, O.J. Kwon, Electrodeposition of Cu-Ag Film in Cyanide-Based Electrolyte, ECS Trans 33 (2011) 5–10. https://doi.org/10.1149/1.3557565.

[38]    Y. Jeon, S. Choe, H.C. Kim, M.J. Kim, J.J. Kim, Electrodeposition of Cu-Ag films in ammonia-based electrolyte, J Alloys Compd 775 (2019) 639–646. https://doi.org/10.1016/j.jallcom.2018.10.023.

[39]    N.J. Bunce, D. Bejan, Mechanism of electrochemical oxidation of ammonia, Electrochim Acta 56 (2011) 8085–8093. https://doi.org/10.1016/j.electacta.2011.07.078.

[40] J.A. Hammons, T. Muselle, J. Ustarroz, M. Tzedaki, M. Raes, A. Hubin, H. Terryn, Stability, assembly, and particle/solvent interactions of Pd nanoparticles electrodeposited from a deep eutectic solvent, Journal of Physical Chemistry C 117 (2013) 14381–14389. https://doi.org/10.1021/jp403739y.

[41] E. Plaza-Mayoral, P. Sebastián-Pascual, K.N. Dalby, K.D. Jensen, I. Chorkendorff, H. Falsig, M. Escudero-Escribano, Preparation of high surface area Cu-Au bimetallic nanostructured materials by co-electrodeposition in a deep eutectic solvent, Electrochim Acta 398 (2021) 139309. https://doi.org/10.1016/j.electacta.2021.139309.

[42] E. Plaza-Mayoral, I.J. Pereira, K. Nicole Dalby, K.D. Jensen, I. Chorkendorff, H. Falsig, P. Sebastián-Pascual, M. Escudero-Escribano, Pd-Au Nanostructured Electrocatalysts with Tunable Compositions for Formic Acid Oxidation, ACS Appl Energy Mater 5 (2022) 10632–10644. https://doi.org/10.1021/acsaem.2c01361.

[43] P. Guillamat, M. Cortés, E. Vallés, E. Gómez, Electrodeposited CoPt films from a deep eutectic solvent, Surf Coat Technol 206 (2012) 4439–4448. https://doi.org/https://doi.org/10.1016/j.surfcoat.2012.04.093.

[44] J.C. Malaquias, M. Steichen, M. Thomassey, P.J. Dale, Electrodeposition of Cu-In alloys from a choline chloride based deep eutectic solvent for photovoltaic applications, Electrochim Acta 103 (2013) 15–22. https://doi.org/10.1016/j.electacta.2013.04.068.

[45] E. Gómez, A. Fons, R. Cestaro, A. Serrà, Electrodeposition of CoNi alloys in a biocompatible DES and its suitability for activating the formation of sulfate radicals, Electrochim Acta 435 (2022). https://doi.org/10.1016/j.electacta.2022.141428.

[46] M. Steichen, M. Thomassey, S. Siebentritt, P.J. Dale, Controlled electrodeposition of Cu-Ga from a deep eutectic solvent for low cost fabrication of CuGaSe2 thin film solar cells, Physical Chemistry Chemical Physics 13 (2011) 4292–4302. https://doi.org/10.1039/c0cp01408g.

[47] A. Liu, Z. Shi, R.G. Reddy, Mechanism study of Cu-Zn alloys electrodeposition in deep eutectic solvents, Ionics (Kiel) 26 (2020) 3161–3172. https://doi.org/10.1007/s11581-019-03418-2.

[48] R. Bernasconi, G. Panzeri, G. Firtin, B. Kahyaoglu, L. Nobili, L. Magagnin, Electrodeposition of ZnNi Alloys from Choline Chloride/Ethylene Glycol Deep Eutectic Solvent and Pure Ethylene Glycol for Corrosion Protection, Journal of Physical Chemistry B 124 (2020) 10739–10751. https://doi.org/10.1021/acs.jpcb.0c04784.

[49] A.P. Abbott, A.I. Alhaji, K.S. Ryder, M. Horne, T. Rodopoulos, Electrodeposition of copper-tin alloys using deep eutectic solvents, Transactions of the Institute of Metal Finishing 94 (2016) 104–113. https://doi.org/10.1080/00202967.2016.1148442.

[50] M. Manolova, R. Böck, I. Scharf, T. Mehner, T. Lampke, Electrodeposition of Pd alloys from choline chloride/urea deep eutectic solvents, J Alloys Compd 855 (2021) 157462. https://doi.org/https://doi.org/10.1016/j.jallcom.2020.157462.

[51] J. Huang, W. Wang, Q. Xiang, S. Qin, P. Wang, N. Mitsuzaki, Z. Chen, Effect of deposition potential on electrodeposition of Sn-Ag-Cu ternary alloy solderable coating in deep eutectic solvent, Journal of Electroanalytical Chemistry 943 (2023). https://doi.org/10.1016/j.jelechem.2023.117613.

[52]   P. Sebastián, E. Vallés, E. Gómez, Copper electrodeposition in a deep eutectic solvent. First stages analysis considering Cu(I) stabilization in chloride media, Electrochim Acta 123 (2014) 285–295. https://doi.org/10.1016/j.electacta.2014.01.062.

[53]   P. Sebastián, E. Vallés, E. Gómez, First stages of silver electrodeposition in a Deep Eutectic Solvent. Comparative behavior in aqueous medium, n.d.

[54]   P. Sebastián, E. Torralba, E. Vallés, A. Molina, E. Gómez, Advances in Copper Electrodeposition in Chloride Excess. A Theoretical and Experimental Approach, Electrochim Acta 164 (2015) 187–195. https://doi.org/10.1016/j.electacta.2015.02.206.

[55]   A.P. Abbott, M. Azam, K.S. Ryder, S. Saleem, Study of silver electrodeposition in deep eutectic solvents using atomic force microscopy, Transactions of the Institute of Metal Finishing 96 (2018) 297–303. https://doi.org/10.1080/00202967.2018.1520483.

[56]   H.R. Ghenaatian, M. Shakourian-Fard, G. Kamath, Interaction of Cun, Agn and Aun (n = 1–4) nanoparticles with ChCl:Urea deep eutectic solvent, J Mol Graph Model 105 (2021). https://doi.org/10.1016/j.jmgm.2021.107866.

[57]   A.D. Ballantyne, R. Barker, R.M. Dalgliesh, V.C. Ferreira, A.R. Hillman, E.J.R. Palin, R. Sapstead, E.L. Smith, N.J. Steinke, K.S. Ryder, Electrochemical deposition of silver and copper from a deep eutectic solvent studied using time-resolved neutron reflectivity, Journal of Electroanalytical Chemistry 819 (2018) 511–523. https://doi.org/10.1016/j.jelechem.2018.01.032.

[58]   M.B. Vukmirovic, R.R. Adzic, R. Akolkar, Copper Electrodeposition from Deep Eutectic Solvents - Voltammetric Studies Providing Insights into the Role of Substrate: Platinum vs Glassy Carbon, Journal of Physical Chemistry B 124 (2020) 5465–5475. https://doi.org/10.1021/acs.jpcb.0c02735.

[59]   Q. Li, H. Qian, X.U. Fu, H. Sun, J. Sun, Characterization and electrochemical analysis of silver electrodeposition in ChCl-urea deep eutectic solvents, (n.d.). https://doi.org/10.1007/s12034-020-02276-3S.

[60]   A.P. Abbott, K. El Ttaib, G. Frisch, K.J. McKenzie, K.S. Ryder, Electrodeposition of copper composites from deep eutectic solvents based on choline chloride, Physical Chemistry Chemical Physics 11 (2009) 4269–4277. https://doi.org/10.1039/b817881j.

[61]   P. Sebastián-Pascual, M. Escudero-Escribano, Surface characterization of copper electrocatalysts by lead underpotential deposition, Journal of Electroanalytical Chemistry 896 (2021). https://doi.org/10.1016/j.jelechem.2021.115446.

[62]   E. Herrero, L.J. Buller, H.D. Abruña, Underpotential deposition at single crystal surfaces of Au, Pt, Ag and other materials, Chem Rev 101 (2001) 1897–1930. https://doi.org/10.1021/cr9600363.

[63]   J.R. Rumble, D.M. Bickham, C.J. Powell, The NIST x-ray photoelectron spectroscopy database, Surface and Interface Analysis 19 (1992) 241–246. https://doi.org/10.1002/sia.740190147.

[64]   N. Pauly, S. Tougaard, F. Yubero, Determination of the Cu 2p primary excitation spectra for Cu, Cu 2O and CuO, Surf Sci 620 (2014) 17–22. https://doi.org/10.1016/j.susc.2013.10.009.

[65]  D. Tahir, S. Tougaard, Electronic and optical properties of Cu, CuO and Cu 2O studied by electron spectroscopy, Journal of Physics Condensed Matter 24 (2012). https://doi.org/10.1088/0953-8984/24/17/175002.

[66]  J. Leiro, E. Minni, E. Suoninen, Study of plasmon structure in XPS spectra of silver and gold, 1983. http://iopscience.iop.org/0305-4608/13/1/024.

[67]  N. Pauly, F. Yubero, S. Tougaard, Quantitative analysis of satellite structures in XPS spectra of gold and silver, Appl Surf Sci 383 (2016) 317–323. https://doi.org/10.1016/j.apsusc.2016.03.185.

[68]  H. Liao, A. Fisher, Z.J. Xu, Surface Segregation in Bimetallic Nanoparticles: A Critical Issue in Electrocatalyst Engineering, Small 11 (2015) 3221–3246. https://doi.org/10.1002/smll.201403380.

[69]  T. Chierchie, C. Mayer, Voltammetric study of the underpotential deposition of copper on polycrystalline and single crystal palladium surfaces, Electrochim Acta 33 (1988) 341–345. https://doi.org/10.1016/0013-4686(88)85026-6.